Unravelling the structural and chemical features influencing deformation-induced martensitic transformations in steels

G. K. Tirumalasetty[1,2*], M.A. van Huis[2,3], C. Kwakernaak[4],

J. Sietsma[4], W.G Sloof[4], H.W. Zandbergen[2*]

[1] *Materials innovation institute (M2i), Mekelweg 2, 2628 CD Delft, The Netherlands*

[2] *Kavli Institute of Nanoscience, Delft University of Technology, Lorentzweg 1, 2628 CJ Delft, The Netherlands*

[3]*Soft Condensed Matter, Debye Institute for Nanomaterials Science, Utrecht University, Princetonplein 5, 3584 CC Utrecht, The Netherlands*

[4]*Department of Materials Science and Engineering, Delft University of Technology, Mekelweg 2, 2628 CD Delft, The Netherlands*

[*]Corresponding author:

Address: Kavli Institute of Nanoscience,
Delft University of Technology,
Lorentzweg 1, 2628 CJ Delft,
The Netherlands

Email: ganeshkumar.india@gmail.com.

Tel./ fax: +31 15 2781536 / +31 15 2786600.

Abstract

A combination of Electron Back-Scattered Diffraction (EBSD) and high-sensitivity Electron Probe Micro-Analysis (EPMA) was used to correlate the changes in microstructural features upon deformation with local chemical composition in Transformation-Induced Plasticity steels. A novel cleaning procedure was developed that allows complete monitoring of transformation and deformation processes in relation to the local crystal structure, microstructure and chemical composition. Here we show direct evidence that local variations in manganese content enable a gradual transformation of the retained austenite grains.

Keywords: Transformation-Induced Plasticity (TRIP) steel; Electron back-scattered diffraction (EBSD); Electron probe microanalysis (EPMA); chemical mapping; martensitic transformation.

The intriguing phenomenon of martensitic (diffusionless) phase transformations occurring during deformation was recognized by Sauveur [1] in 1924 by means of his torsion tests on iron bars. Surprisingly, it led to a substantial increase in ductility and the effect was later termed transformation-induced plasticity (TRIP) [2]. The first practical exploitation of the TRIP effect came in 1967 from Zackay and coworkers, who developed steels with dramatically improved elongation as a consequence of the deformation-induced martensitic transformation [3]. Considerable scientific and technological interest grew in the early 1970s in the field of zirconia-containing ceramics exhibiting such phase transformations [4]. The concept of deformation-induced phase transformation has also been applied to polymers [5], brittle bulk metallic glasses [6] and very recently to titanium-based biomedical alloys [7]. In view of the technological importance there is a strong interest in understanding deformation-induced phase transformations, in particular to assess the role of various microstructural parameters such as the local chemical composition [8], grain size [9], crystal lattice orientation in relation to strain direction [10] and the location of the grain in relation to its surrounding grains [11]. An accurate understanding of all these factors and their interplay will allow fine tuning of phase transformations resulting in an enhanced control over the material properties [12].

Despite the fact that steels are amongst the most extensively investigated materials, many features of the martensitic transformation process during deformation remain unclarified to date. In particular the role of alloying elements such as C, Mn, Si, and Al during transformations is poorly understood [13] and there is an increasing need to gain fundamental insights into this topic. In this study, two steels with chemical

composition (wt.%) Fe−1.65Mn−1.53Si −0.037Al−0.199C (Si-alloyed TRIP steel) and Fe−1.62Mn−0.35Si−0.91Al−0.187C (Al-alloyed TRIP steel) are investigated. Both these steels are commercially produced on an industrial hot dip galvanizing line using a conventional intercritical annealing cycle followed by cooling to around 400–460°C, isothermally holding it at this temperature and finally cooling it to room temperature.

In order to obtain combined information of the crystallographic structure, orientation, and chemical composition of each grain in relation to its neighbouring grains, and their changes upon an overall deformation and the strain direction, we have used a combination of two techniques: EBSD and EPMA. EBSD enables to monitor the microstructural changes of individual grains during deformation. For instance, we recently reported an EBSD study showing that metastable austenite grains rotate within the matrix (of ferrite) during the tensile tests in TRIP steels [11], thereby contributing to the high ductility of these steels. EPMA is a very reliable analytical technique to measure the chemical composition. Although EBSD and EPMA can provide the required information, their actual application for monitoring phase transformations is hampered by an inevitable formation of carbon contamination on the surface. This carbon layer is deposited during the measurements due to decomposition of residual hydrocarbon gases [14] by the electron beam, which deteriorates the quality of EBSD data and makes the EPMA carbon content analysis totally unreliable.

It is thus essential to remove the contamination formed during each EBSD and EPMA measurement, prior to additional EBSD or EPMA experiments performed after straining. For this purpose, we have successfully developed a two-step plasma cleaning procedure, using a very low-energy oxygen plasma followed by a hydrogen radicals

plasma (details in the Supporting Information (SI)). The key component is the use of low-energy hydrogen radicals, which can only result in chemical processes at the surface [15] instead of the generally used physical sputtering. We obtained excellent results using first oxygen-plasma cleaning for 3 minutes followed by hydrogen-plasma cleaning for 40 minutes. The EBSD data after cleaning showed the same quality as the EBSD data on the virgin surface: in both cases 85% of the EBSD patterns could be indexed, whereas with the carbon contamination layer only 10% could be indexed, and with oxygen plasma cleaning alone only 30% could be indexed.

A schematic of the sample and the EBSD and EMPA measurements is shown in Figure 1. Dog-bone samples were electropolished in order to have a surface layer that is not mechanically deformed. Markers were created by indentation with a Vickers indenter, and EBSD and EPMA mapping was performed between these markers. Scanning electron microscopy (SEM) images were recorded before and after EBSD measurements to track the respective locations. The samples were plasma-cleaned after each EBSD or EMPA analysis using the cleaning procedure described above. After the EBSD and EPMA measurements the samples were deformed and EBSD maps were recorded again on the same area. The samples were only lightly strained to follow the first transformations during the deformation process. SEM-EBSD was performed using a JEOL JSM 6500F operated at 20 kV, and EPMA was performed using a JEOL JXA 8900R microprobe operated at 10 kV with a spot size of 500 nm (more experimental details in SI).

Figure 3A and Figure S2A shows a typical TRIP steel microstructure consisting of ferrite matrix (coloured green) and metastable grains of retained austenite

(coloured red). Retained austenite having a face centred cubic (fcc) structure and ferrite having a body centred cubic (bcc) structure can easily be distinguished by EBSD software as they have different crystallographic structures. Grains of martensite, grain boundaries, and areas with high dislocation density are not indexed by the EBSD software due to the poor quality of the Kikuchi patterns and are imaged in black in the phase identification maps. An EPMA line scan was performed on the EBSD mapped regions as shown in Figure 3A, Figure S2A and the corresponding elemental compositions of retained austenite grains are plotted in Figures 3C-E, Figure S2C-E. Among all austenite grains intersected by the EPMA line scan, it is clear from Figure S2B that grains a4-UT and a7-UT remain untransformed (UT), whereas grains a5-CT, a6-CT and a8-CT are completely transformed (CT) after deformation. Strikingly, EPMA chemical composition maps in Figure S2C showed that grains a4-UT and a7-UT contained very low manganese (Mn) concentrations and grains a5-CT, a6-CT and a8-CT contained relatively very high Mn concentrations. Furthermore, Figure S2D showed that grains a4-UT and a7-UT contained fairly high silicon (Si) concentrations. This contradicts the existing experimental literature on steels, [16][17]which suggests that lower Mn and higher Si contents should destabilize the austenite and lead to an early onset of martensitic transformation.

In the literature several factors affecting the martensitic transformation are given: (1) the local carbon concentration in austenite, [8] (2) the grain size of the austenite grains, [9] (3) the crystallographic orientation of austenite grains with respect to the loading direction, [10] and (4) the position of the austenite grains within the ferrite matrix [11]. The above four factors were also closely assessed for these grains with the

help of EBSD and EPMA analysis. Regarding the effect of carbon concentration, the EPMA maps in Figure S2E clearly show that grain a4-UT had a very low carbon concentration, which should facilitate transformation. Regarding the grain size effect, grain a7-UT has a very large grain size, which should result in early transformation. Regarding the crystallographic effect, the Schmid factors (see SI) can be used to predict the ease of transformation based on the crystallographic orientation of a given grain to the strain direction. It is clear from Figures S3A and S3B that grains a4-UT and a7-UT exhibit different orientations, whereby a7-UT has a higher Schmid factor, which should promote easy slip and assist the transformation of this grain. Regarding the effect of the location of the austenite grain, grain a4-UT, which is located at the grain boundary, should facilitate an early transformation. In view of all the above observations we conclude that both Mn and or Si majorly influence the transformation of the austenite grains in this steel.

Aluminium (Al) is another element that can influence the transformation behaviour [18]. The Si-alloyed TRIP steel shown in Figure S2 has a very low Al content, and therefore we investigated an Al-alloyed TRIP steel as well. The EBSD–EPMA results are displayed in Figure 3. As observed in panels 3C and 3D, the Al and Si contents do not have a major influence on the transformation. However, we find a consistent trend that austenite grains having higher Mn contents (Figure 3E) transform earlier during the deformation process. The transformation behaviour of all the austenite grains and various parameters influencing the transformation is summarized in Table S1. We conclude that local Mn contents in austenite grains strongly influence the transformation in both TRIP steels.

The results clearly show that Mn-rich austenite grains transform earlier during the deformation process. As Mn stabilises austenite [17], it cannot be a thermodynamic effect and must be kinematic in nature, thus local configurations must lower the energy barrier for the transformation. Possible reasons for the faster transformation of Mn-rich austenite grains can be (a) enhanced strain at the grain boundaries due to Mn segregation (b) internal additional stresses due to variations in Mn concentrations within the grain, or (c) the twin boundaries that were observed in some (about 20%) of the Mn-rich austenite grains (Figures S3-S5). In order to verify these issues, we performed a chemical analysis on a twinned austenite grain using energy-dispersive X-ray spectrometry (EDX) within the transmission electron microscope (TEM), using a Tecnai 20F operated at 200 kV (details in SI). The results are shown in Figure 4. Our analysis shows no Mn enrichment at the austenite–ferrite grain boundary, nor at the twin boundaries of austenite grains. However, a clear inhomogeneous distribution of Mn (with local variations in concentration up to 40–50%) was observed within the twinned austenite grain. The variation in Mn content is also consistent with the EPMA concentration maps (Figure S2) of some of the transformed grains without twin faults. We propose that Mn variations within the austenite grain cause the early martensitic nucleation. At a very local scale, substitution of Fe by Mn leads to a lattice increase, [19] which can result in local strain acting as a trigger for transformation. Once started, the transformation proceeds at high speed (~2 times the speed of sound) [16], resulting in a full transformation to martensite.

Experimental studies [20] indicate that the total collection of retained austenite grains (in the limit of one by one) should transform gradually during the tensile deformation so as to delay the onset of necking and micro-crack initiation, which leads to

an extended ductility in these materials. Here we show that by variation of the manganese concentration, in combination with microstructural parameters such as grain size, orientations and positioning of grains within the ferritic matrix, the occurrence of phase transformations can be "designed" such that they occur sequentially, which leads to desirable properties. Furthermore, our results show the need for detailed models, taking not only the thermodynamics into account but certainly also the kinetics, whereby the effects of local variations in concentration on the scales of 100 nm as well as several microns should be included, as well as modelling for the optimum size and shape of the grains. From a technological and scientific perspective, these results calls for a revisit of systems studied, in particular by examining the local composition, because there is a strong interrelation between the local composition, the microstructure and mechanical properties.

This research was funded by the Materials innovation institute M2i (project nr. MC5.06280a). The authors thank F.T. Molkenboer, N.B. Koster (TNO), G. Schneider for plasma cleaning, S.R.K Malladi, M. Neklyudova for STEM-EDX, and N.H. van Dijk, S. Turteltaub, B.J. Thijsse (DUT) for useful discussions. We thank Dr. D.N. Hanlon (Tata Steel RDT) for providing sample material and constructive discussions.

[1] A. Sauveur, Iron Age. 113 (1924) 581.
[2] M. De Jong & GW. Rathenau, Nature 181 (1958) 1396–1397.
[3] V.F. Zackay, E.R. Parker, D. Fahr, R Bush, Trans ASM. 60 (1967) 252–259.
[4] R.C. Garvie, , R.T. Pascoe, R.H.J. Hannink, Nature 258 (1975) 703−705.
[5] F. Auriemma, C. De Rosa, S. Esposito, G.R. Mitchell, Angew. Chem. 46 (2007) 4325–4328.

[6] Y. Wu, Y.H. Xiao, G.L. Chen, C.T. Liu, Z.P. Lu, Adv Mater. 22 (2010) 2770–2773.

[7] Z. Xiaoli, N. Mitsuo, N. Masaaki, M. Goro, F. Tadashi, Acta Biomater. 7 (2011) 3230–3236.

[8] N.H. Van Dijk, *et al.*, Acta Mater. 53 (2005) 5439–5447.

[9] E. Jimenez-Melero, N.H. van Dijk, L. Zhao, J. Sietsma, S.E. Offerman, J.P. Wright, S. van der Zwaag. Scripta Mater. 56 (2007) 421–424.

[10] S.O. Kruijver, *et al.*, J. Phys. IV. 104 (2003) 499–502.

[11] G.K. Tirumalasetty, M.A. van Huis, C. Kwakernaak, J. Sietsma, W.G. Sloof, H.W. Zandbergen, Acta Mater. 60 (2012) 1311–1321.

[12] S.E. Offerman, *et al.* Science 298 (2002) 1003-1005.

[13] M.A. Militzer. Science 298 (2002) 975–976.

[14] A.V. Crewe, Science 154 (1966) 729–738.

[15] N.B. Koster, J.C.J. van der Donck, J.K. Stortelder, A.J. de Jong, F.T. Molkenboer Proc. SPIE, Vol 8322 (2012) 83220R.

[16] N. Nishiyama, *Martensitic Transformation*, Ch, 4. Academic press. New York, 1978.

[17] W.F. Smith, *Structure and Properties of Engineering Alloys*, Ch 4. McGraw-Hill. New York, 1993.

[18] B.C. De Cooman, Current Opinion in Solid State and Materials Science. 8 (2004) 285–303.

[19] A. Dick, T. Hickel, Neugebauer, J Steel Res. Inter. 80 (2009) 603–608.

[20] H.C. Chen, H. Era, M. Shimizu, Metall. Trans. A. 20A (1989) 437–445.

Figure 1

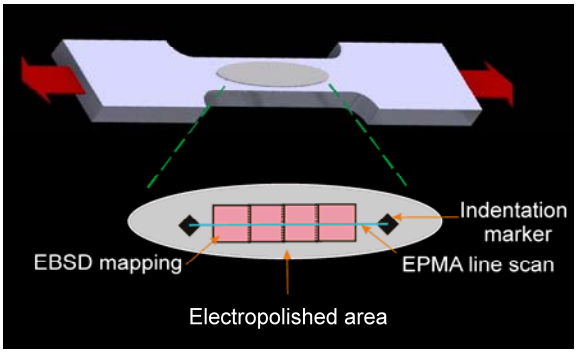

Fig 1: Schematic of dog-bone TRIP steel sample subjected to tensile deformation. The inset shows the central electropolished area where adjacent EBSD maps and an EPMA line scan are recorded between markers. The indentation markers are also visible in the experimental SEM images (Figure 2). Experimental details are given in the SI.

Figure 2

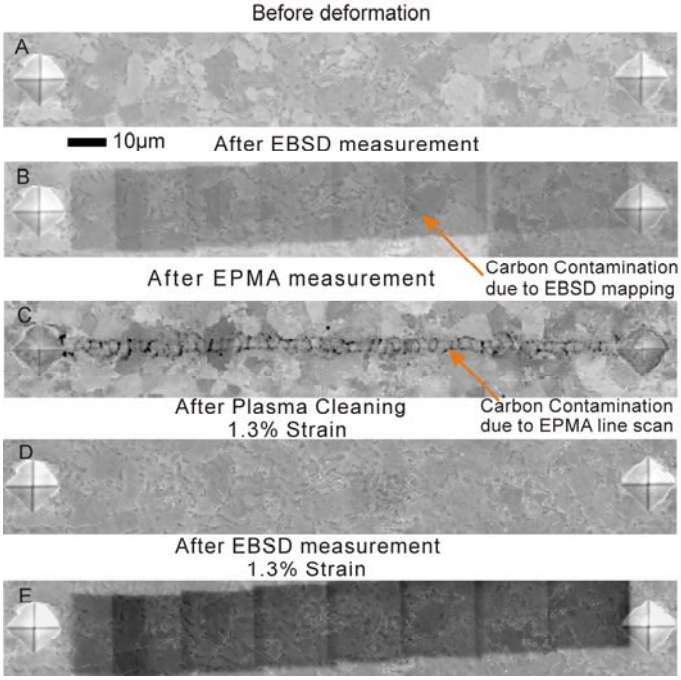

Fig 2: (A,B,D,E) SEM and (C) back-scattered EPMA image of Al-alloyed TRIP steel indicating carbon contamination caused by EBSD mapping (B,E) and by the EPMA line scan (C). (D) Removal of carbon contamination by plasma cleaning.

Figure 3

Fig 3: EBSD phase identification maps of Al-alloyed TRIP steel showing retained austenite grains labelled (c1-c9, d1-d9, e1-e9, f1, f2) (A) before and (B) after deformation and EPMA composition profile of (C) aluminium, (D) silicon and (E) manganese corresponding to retained austenite grains. (F) Inverse-pole figure map showing austenite grain C2 with a twin fault. Accuracies are given in Table S2 (SI).

Figure 4

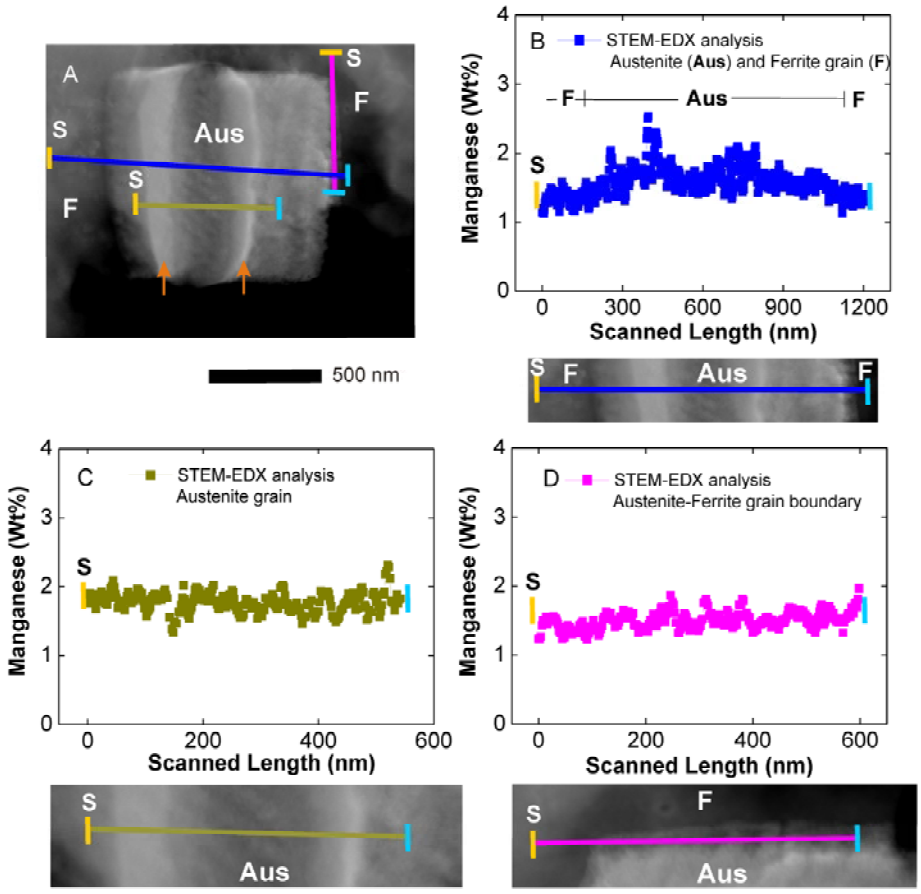

Fig 4: (A) TEM micrograph of Si-alloyed TRIP-assisted steel showing a twinned austenite grain (Aus) within the ferrite matrix (F). (B,C) STEM-EDX composition profile and corresponding TEM image of ferrite (B) and austenite (C) grains, and the austenite-ferrite grain boundary (D). The gold marker (S) indicates the start and cyan the end point of the EDX line scans. Orange arrows indicate the position of twin boundaries.

- Supporting Information -

Unravelling the structural and chemical features influencing deformation-induced martensitic transformations in steels

G. K. Tirumalasetty, M.A. van Huis, C. Kwakernaak,

J. Sietsma, W.G. Sloof, H.W. Zandbergen

Methods

Sample preparation. Dog-bone samples were prepared by spark erosion keeping the long axis along the rolling direction. The sample dimensions are shown in Figure S1a. Samples were grinded and electropolishing was performed with freshly prepared electrolyte with a composition of 100 ml perchloric acid and 300 ml butanol in 500 ml methanol at 20 V and 10°C for 20 seconds. The electropolished samples were marked as shown in Figure 1 with small Vickers indentations with an applied load of 0.12 N to serve as reference points of EBSD patterns and for the EPMA line scan (Figure 2). It was also used to determine the local strain of the sample. The indentations were made 150 μm apart and EBSD mapping was performed between the indentations.

Tensile testing experiments were performed with a 5 kN Deben Microtest tensile stage, which was controlled by dedicated Microtest software from Deben. The tensile tests were executed with a constant deformation rate of 1.2×10^{-3} s^{-1}. The local permanent strain experienced by the samples was calculated by measuring the distance between the indentations before and after the tensile test.

Electron back-scattered diffraction (EBSD) was performed using a JEOL JSM 6500F Schottky field emission gun scanning electron microscope (FEG-SEM) equipped with an

HKL Nordlys II detector operated with Channel 5 software. A 20-keV focused electron beam with a beam current of approximately 1 nA was applied. The adjacent EBSD maps shown in Figs. 1 and 2 were stitched together using Map Stitcher software. The normal of the sample surface at a working distance of 25 mm was tilted to 70º with respect to the electron beam towards the EBSD detector. The ellipsoid beam spot size was estimated to be 10 × 25 nm^2. The distinction between the austenitic face centred cubic (fcc) and ferritic body centred cubic (bcc) phases was straightforward when 9 Kikuchi bands were used to analyze the diffraction patterns. From the Kikuchi patterns, the corresponding orientation of each crystal lattice was determined with the Channel 5 software from HKL Technology developed by Oxford Scientific Instruments. Knowing the rolling (RD), transverse (TD) and normal (ND) directions of the sample, we generated inverse pole figure maps and Schmid factor maps from the EBSD software. Inverse pole figure maps help for analysis of the grain orientations, while the Schmid factors map indicates the relative susceptibility of each grain to deformation slip. In fcc metals, it is well known that dislocation movement occurs in four {111} slip planes with three possible <110> slip directions. Hence, 12 possible slip systems were considered for austenite. The grains having a higher Schmid factor are indicated in red, whereas those with a very low Schmid factor are indicated in blue using rainbow colouring. To avoid strain-aging effects each sample was deformed only once to a desired level of strain.

Electron probe micro analysis (EPMA) was performed using a JEOL JXA 8900R microprobe with a spot size of 500 nm (electron beam energy 10 keV, beam current 50 nA), employing wavelength dispersive spectrometry (WDS). The points of analysis were located along lines 150 μm in length with increments of 0.5 μm at which the contents of C, Mn, Si and Al were measured. The obtained intensity ratios were processed with a matrix correction program CITZAF [21]. The composition at each analysis location of the sample was determined according to the X-ray intensities relating to the constituent elements after background correction relative to the corresponding intensities of reference materials. The reference materials used were cementite (Fe_3C) for carbon and the pure elements for the other elements (Astimex MM44-25). An air jet was used to decontaminate the sample surface and prevent the deposition of carbonaceous substances.

Prior to the measurement, the spot was decontaminated for 30 seconds, followed by the actual measurement for 120 seconds. The analysis depth at every measurement location was 200 nm. In order to avoid the positional errors due to the electron beam drift, the equipment was stabilized for 2 hours before the measurements.

Transmission electron microscopy (TEM). Electron transparent TEM samples were prepared using standard electropolishing to reveal various phases in the TEM microstructures. The samples for transmission electron microscopy (TEM) were mechanically pre-thinned along the ND-TD plane using SiC paper with roughness from 350 down to 4000. Electropolishing was thereafter carried out in a twin-jet polisher using 5 percent perchloric acid solution at a temperature of -20^0C [22]. TEM analysis was performed using Philips CM30T and FEI Tecnai F20ST/STEM microscopes operating at 300 and 200 kV, respectively. Selected Area Diffraction (SAD) was used to distinguish austenite and ferrite phases while Scanning Transmission Electron Microscopy - Energy Dispersive X-ray spectrometry (STEM-EDX) was employed to investigate chemical compositions.

Novel plasma cleaning procedure. The cleaning procedure was optimized by varying the durations of the sequential oxygen and hydrogen plasma exposures. Oxygen plasma cleaning was performed using Spi plasma prep II operating at 13.4 GHz and a power of 100 Watts. Shielded microwave-induced remote plasma (SMIRP) was used for hydrogen plasma cleaning. The plasma was excited using a radio frequency generator with 2.4 GHz and the plasma power was set at 1000 Watts with a duty cycle of 50%.

Fine-tuning of the plasma cleaning procedure. Our initial EBSD experiments with TRIP 800 steels showed a Kikuchi pattern indexing of about 87%. EBSD followed by EPMA on the same area resulted in indexing of only 10% due to extensive carbon deposition on the surface of the sample. Oxygen plasma cleaning was performed for 10 minutes and it was very effective in removing the entire carbon contamination. It is well known that ultraviolet light generated in the plasma effectively breaks the organic bonds of surface contaminants and that the energetic oxygen species created in the plasma react

with organic contaminants to form mainly water and carbon dioxide, which are continuously pumped away from the chamber during the cleaning process [23]. Nevertheless, the process leads to visible tanning due to oxidation of the steel surface and marked deterioration in the quality of Kikuchi patterns, yielding close to 30% indexing. Plasma cleaning on another sample with hydrogen for 90 minutes showed about 60% indexing with some remains of carbon on the sample surface. Strikingly, cleaning a sample briefly with oxygen plasma followed by hydrogen plasma resulted in the complete removal of carbon contamination and, more importantly, yielded close to 85% indexing of Kikuchi patterns. Visible reduction in tanning was also observed after hydrogen plasma cleaning so that the hydrogen probably reduced the oxygen at the surface of the sample [24]. An optimal setting was found, whereby the samples were cleaned with oxygen plasma for 3 minutes followed by hydrogen plasma for 40 minutes. The SEM images obtained before and after plasma cleaning can be seen in Figure 2 of the main text. We remark that EBSD/EPMA results shown in Figure 3 correspond to the SEM images in Figure 2. Since our main aim with the Al- alloyed TRIP steel is to understand the role of Mn, Al, and Si we have neglected C in the analysis. Furthermore, the EPMA measurements were carried out with the air jet operated at 40% efficiency, which led to carbon contamination during the EPMA measurements (Figure 2C). Nevertheless, the novel plasma cleaning approach as explained above was very effective in removing the contamination caused by the EPMA line scan measurements which enabled us to follow austenite phase transformation behaviour before and after deformation (Figure 2D).

References

[21] J.T. Armstrong, K.F.J. Heinrich, D.E. Newbury, *Electron Probe Quantitation*, Plenum Press. New York, 1991.

[22] G.K. Tirumalasetty, M.A. van Huis, C.M. Fang, Q. Xu, F.D. Tichelaar, D.N. Hanlon, J. Sietsma, H.W. Zandbergen, Acta Mater. 59 (2011) 7406-7415.

[23] M.A. Hozbor, W.P. Hanse, M. McPherson, Precision Cleaning (1994) 46.

[24] P. Fuchs, Applied Surface Science 256, (2009) 1382–1390.

Table S1: Factors influencing austenite stability which lead to transformation, extracted from figures 3, S3 and S4 (●-untransformed grain, △-fully transformed grain, ◭-partially transformed grain).

Austenite grain number	High Manganese content	Low carbon content	Large grain size	High Schmid factor	Positioned at the Ferrite grain boundary
a1	◭	◭			◭
a2	◭	◭	◭	◭	
a3	△			△	
a4		●			●
a5	△			△	△
a6	△			△	
a7		●	●	●	
a8	△	△	△	△	△
a9	△			△	
b1	△	△		△	△
b2	◭	◭		◭	
b3		◭		◭	
c1	◭			◭	
c2	◭				
c3	△				
c4	◭				
c5			●	●	●
c6	△		△		△
c7	△				
c8			●	●	
c9	△			△	
d1			●		
d2			●	●	

d3			●		
d4	△		△	△	
d5				●	
d6	△				△
d7				●	
d8	△			△	△
d9					●
e1			●	●	
e2			●	●	
e3					●
e4	◭		◭		◭
e5	△				△
e6	◭				◭
e7	◭				
e8	△				△
e9			●		
f1	◭		◭		
f2	△			△	

Table S2:

The EPMA errors in the individual measurements due to counting statistics are:

Average elemental analysis	Si-alloyed TRIP steel (wt %)	Al-alloyed TRIP steel (wt %)
C	0.026	
Al		0.014
Si	0.044	0.076
Mn	0.099	0.018

Figure S1

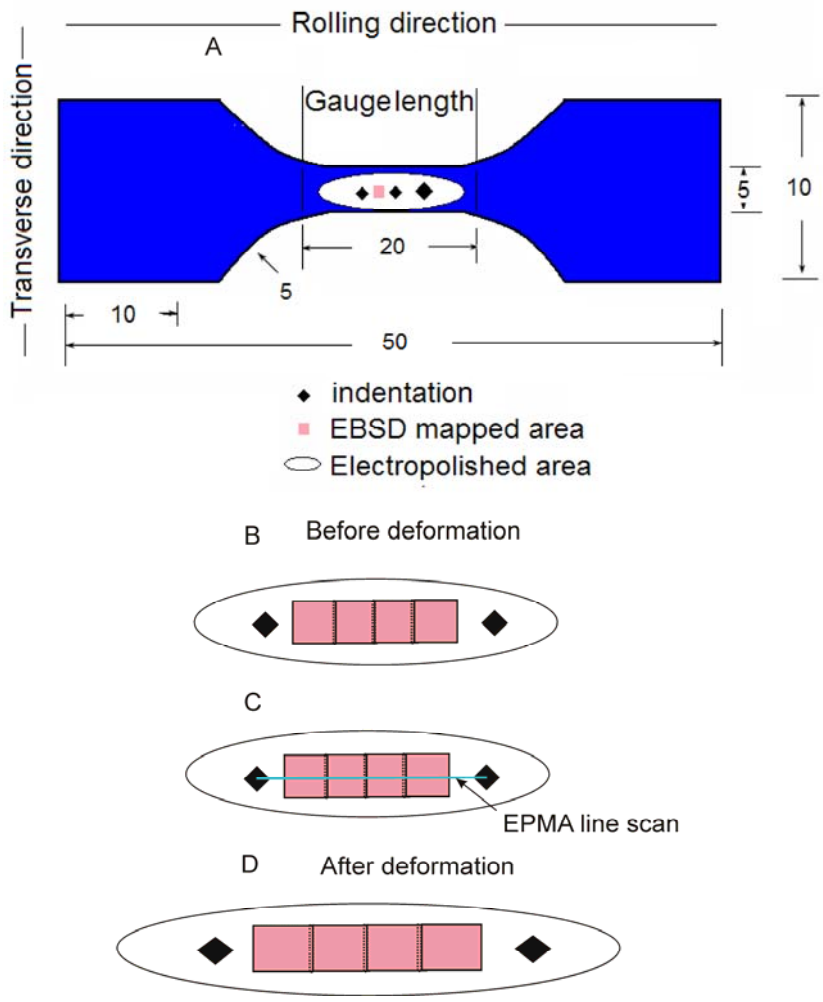

Fig S1: Schematic illustrating the (A) the sample dimensions (mm units). The sequential analysis steps are shown in panels (B)-(D). (B) Enlarged view of the electropolished area with four adjacent EBSD mapped regions; (C) EPMA line scan; (D) EBSD mapping after deformation. Plasma cleaning was performed after every EBSD and EPMA analysis step.

.

Figure S2

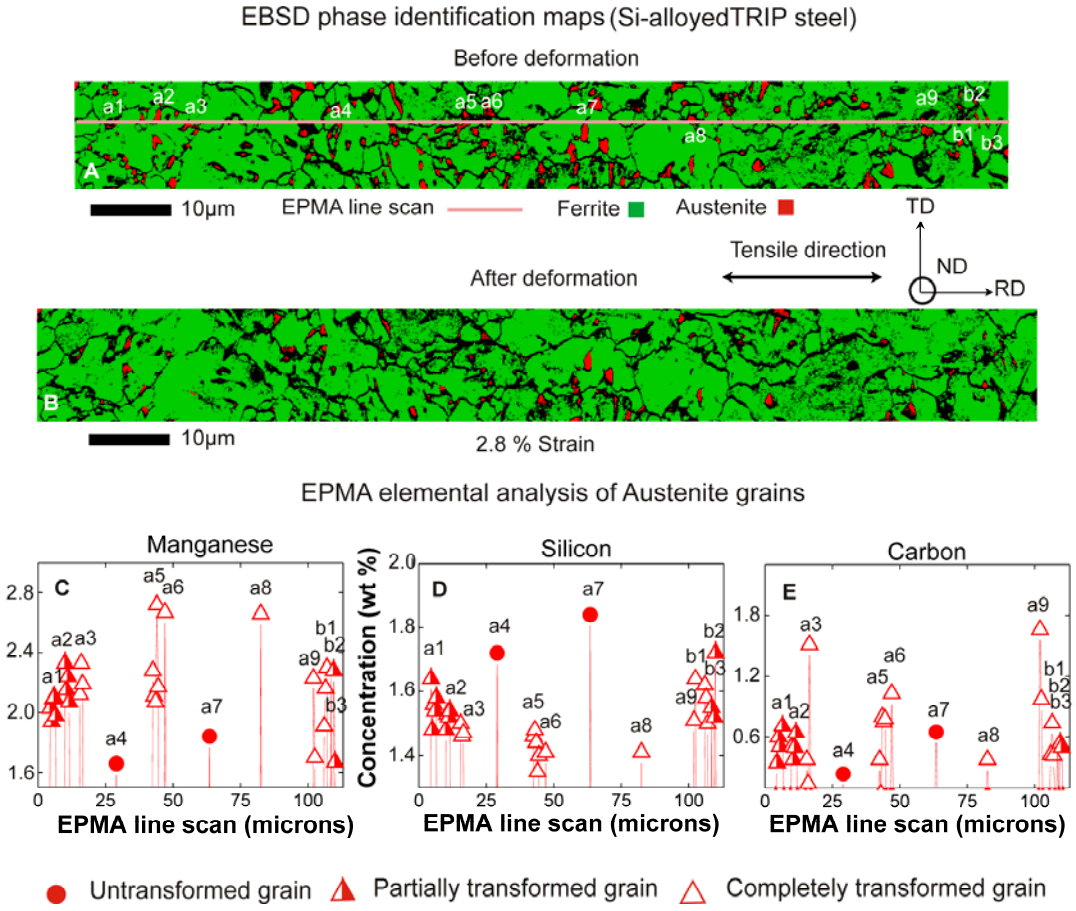

Fig S2: EBSD phase identification maps of Si-alloyed TRIP steel showing retained austenite grains labelled (a1-a9, b1-b3) (A) before and (B) after deformation and EPMA composition profile of (C) manganese, (D) silicon and (E) carbon corresponding to retained austenite grains. The errors in the EPMA measurements can be found in Table S2 of the Supporting Information.

Figure S3

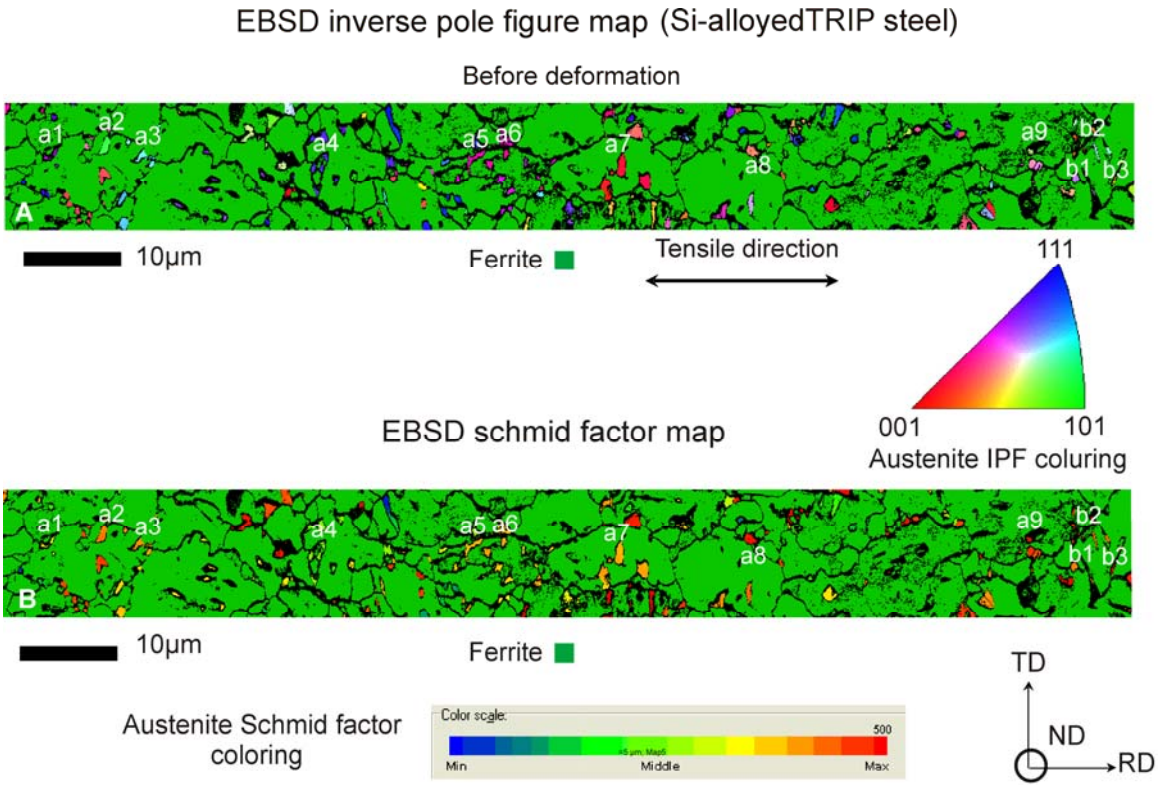

Fig S3: (A) Inverse pole figure map and (B) Schmid factor map of Si-alloyed TRIP steel showing the orientation and Schmid factors of austenite grains before deformation.

Figure S4

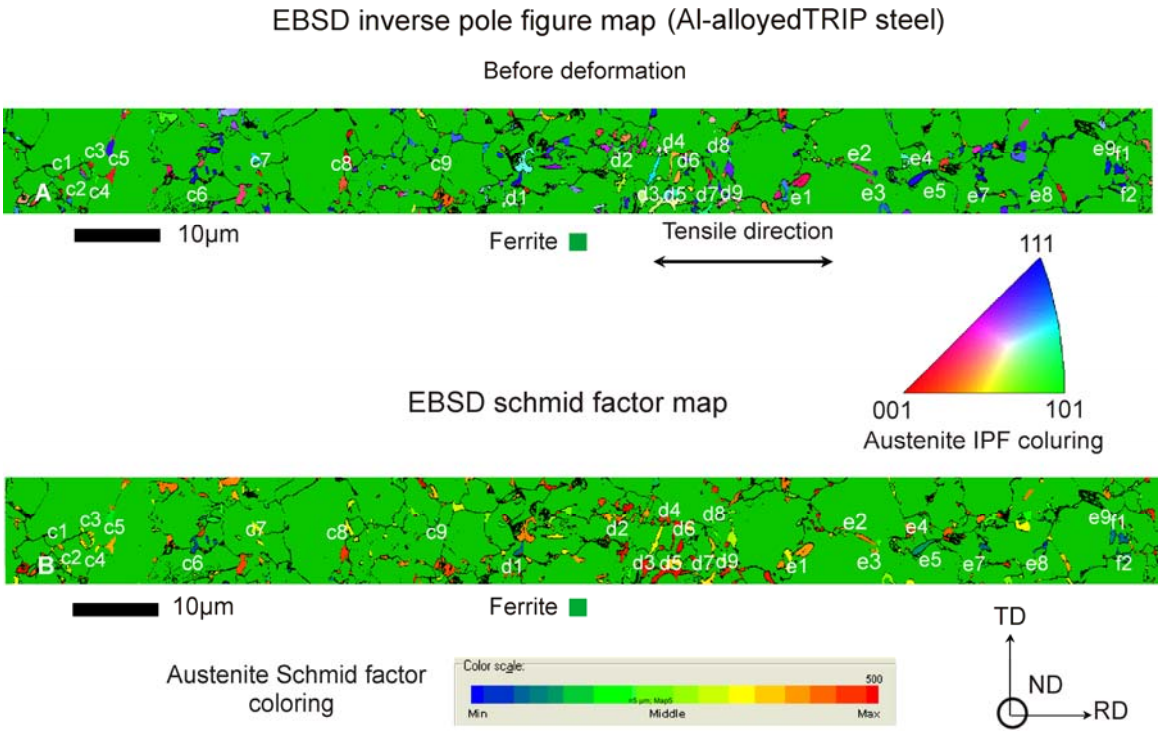

Fig S4: (A) Inverse pole figure map and (B) Schmid factor map of Al-alloyed TRIP steel showing the orientation and Schmid factors of austenite grains before deformation.

Figure S5

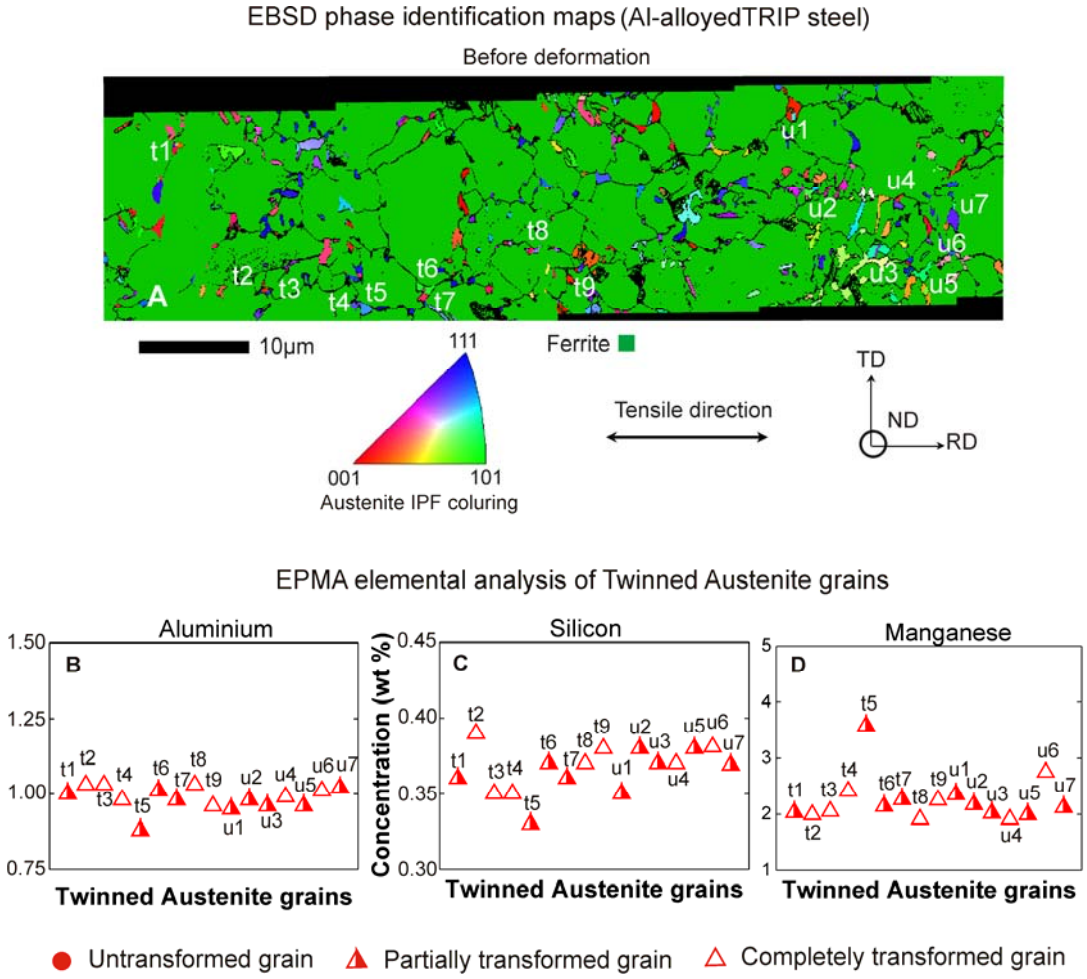

Fig S5: Top: EBSD phase identification maps of the Al-alloyed TRIP steel with the twinned austenite grains labelled as t1-t9 u1-u7. Bottom: corresponding EPMA composition profile of (B) aluminium, (C) silicon and (D) manganese of the retained austenite grains.